minerals

MDPI

Article

Combined In Situ Chemical and Sr Isotopic Compositions and U–Pb Ages of the Mushgai Khudag Alkaline Complex: Implications of Immiscibility, Fractionation, and Alteration

Fan Yang [1], Wei Chen [1,*], Jindrich Kynicky [2,3], Yuancan Ying [1] and Tian Bai [1]

[1] State Key Laboratory of Geological Processes & Mineral Resources, China University of Geosciences, Wuhan 430074, China; yangfan_gpmr@cug.edu.cn (F.Y.); ycyingcug@163.com (Y.Y.); baitian_cug@163.com (T.B.)
[2] BIC Brno, Technology Innovation Transfer Chamber, 61200 Brno, Czech Republic; jindrak@email.cz
[3] Central European Institute of Technology, Brno University of Technology, 61600 Brno, Czech Republic
* Correspondence: wchen@cug.edu.cn; Tel./Fax: +86-027-6788-5096

Abstract: The Mushgai Khudag complex consists of numerous silicate volcanic-plutonic rocks including melanephelinites, theralites, trachytes, shonkinites, and syenites and also hosts numerous dykes and stocks of magnetite-apatite-enriched rocks and carbonatites. It hosts the second largest REE–Fe–P–F–Sr–Ba deposit in Mongolia, with REE mineralization associated with magnetite-apatite-enriched rocks and carbonatites. The bulk rock REE content of these two rock types varies from 21,929 to 70,852 ppm, which is much higher than that of syenites (716 ± 241 ppm). Among these, the altered magnetite-apatite-enriched rocks are characterized by the greatest level of REE enrichment (58,036 ± 13,313 ppm). Magmatic apatite from magnetite-apatite-enriched rocks is commonly euhedral with purple luminescence, and altered apatite displays variable purple to blue luminescence and shows fissures and hollows with deposition of fine-grained monazite aggregates. Most magmatic apatite within syenite is prismatic and displays oscillatory zoning with variable purple to yellow luminescence. Both magmatic and altered apatite from magnetite-apatite-enriched rocks were dated using in situ U–Pb dating and found to have ages of 139.7 ± 2.6 and 138.0 ± 1.3 Ma, respectively, which supports the presence of late Mesozoic alkaline magmatism. In situ $^{87}Sr/^{86}Sr$ ratios obtained for all types of apatite and calcite within carbonatite show limited variation (0.70572–0.70648), which indicates derivation from a common mantle source. All apatite displays steeply fractionated chondrite-normalized REE trends with significant LREE enrichment (46,066 ± 71,391 ppm) and high $(La/Yb)_N$ ratios ranging from 72.7 to 256. REE contents and $(La/Yb)_N$ values are highly variable among different apatite groups, even within the same apatite grains. The variable REE contents and patterns recorded by magmatic apatite from the core to the rim can be explained by the occurrence of melt differentiation and accompanying fractional crystallization. The Y/Ho ratios of altered apatite deviate from the chondritic values, which reflects alteration by hydrothermal fluids. Altered apatite contains a high level of REE (63,912 ± 31,785 ppm), which are coupled with increased sulfur and/or silica contents, suggesting that sulfate contributes to the mobility and incorporation of REEs into apatite during alteration. Moreover, altered apatite is characterized by higher Zr/Hf, Nb/Ta, and $(La/Yb)_N$ ratios (179 ± 48, 19.4 ± 10.3, 241 ± 40, respectively) and a lack of negative Eu anomalies compared with magmatic apatite. The distinct chemical features combined with consistent Sr isotopes and ages for magmatic and altered apatite suggest that pervasive hydrothermal alterations at Mushgai Khudag are most probably being induced by carbonatite-evolved fluids almost simultaneously after the alkaline magmatism.

Keywords: magnetite-apatite-enriched rock; REE mineralization; carbonatite; apatite chemistry; U-Pb ages

Citation: Yang, F.; Chen, W.; Kynicky, J.; Ying, Y.; Bai, T. Combined In Situ Chemical and Sr Isotopic Compositions and U–Pb Ages of the Mushgai Khudag Alkaline Complex: Implications of Immiscibility, Fractionation, and Alteration. *Minerals* **2021**, *11*, 450. https://doi.org/10.3390/min11050450

Academic Editor: Vassily V. Vrublevskii and Anna G. Doroshkevich

Received: 19 February 2021
Accepted: 19 April 2021
Published: 23 April 2021

1. Introduction

Rare earth elements (REEs) are important resources for highly technological applications and are a fundamental component of a range of low- carbon energy production approaches. REEs are included in the recent and current lists of critical metals due to geopolitical controls on their supply [1]. Even though REE mineralization is associated with a range of rocks, including igneous, metamorphic, and sedimentary rocks, alkaline igneous rocks (either carbonatite or syenite) dominate in hosting giant REE deposits [2]. Some examples of these deposits include Bayan Obo (China) [3], Mianning-Dechang (China) [4], Mountain Pass (United States) [5], and Mushgai Khudag (Mongolia) [6]. The Mesoproterozoic Bayan Obo deposit is the largest REE deposit in the world and serves as the main supply for the world's REE market [7]. Compared to the long discovered and investigated Bayan Obo deposit in North China, the petrogenetic and mineralization history of the Mushgai Khudag complex has not been well studied and remains poorly understood. The multi-element REE–Sr–Ba–P–S Mushgai Khudag complex displays complex mineralogical and paragenetic relations, which suggests the occurrence of primary magmatic accumulation modified by hydrothermal processes [2,6,8]. The alkaline complex hosts significant REE–Sr–Ba–P–S mineralization, and REE mineralization is mainly associated with magnetite-apatite-enriched rocks and carbonatites [8–10].

The formation history of the Mushgai Khudag complex has attracted considerable attention. Samoilov and Kovalenko [11] were the first to provide a detailed geological and petrographic description of the complex and put forward its formation sequence. Andreeva et al. [12] inferred that the complex is formed by fractional crystallization and silicate–salt liquid immiscibility based on the chemical compositions of fluid and melt inclusions hosted by silicate minerals (e.g., diopside, garnet, and K-feldspar) in alkaline igneous rocks. Nikolenko et al. [13] presented new Sr–Nd–Pb isotopic compositions as well as geochemical data (LILE/HFSE values), which implies that the parental melts of Mushgai-Khudag were derived from a lithospheric mantle source affected by a mixture of subducted oceanic crust and its sedimentary components. The major and trace element compositions of alkaline silicate rocks suggest that these rocks were formed by fractional crystallization of the nephelinitic parental magma [13].

Magnetite-apatite-enriched rocks within Mushgai Khudag are unique, with the highest apatite contents reaching 80–90 vol.% and REE_2O_3 concentrations in apatite of up to 12 wt.% [10]. Magnetite-apatite-enriched rocks are more commonly known as the dominant component of iron oxide-apatite (IOA) deposits, which are of great economic significance as a source of iron and potential sources of REEs [14]. Magnetite-apatite-enriched rocks are characterized by variable concentrations of apatite (1–50 vol.%) within IOA deposits. These are commonly associated with (sub-)volcanic rocks in convergent margins and rift-related environments [15,16]. The processes involved in the formation of IOA deposits continue to be a controversial topic, with both magmatic and hydrothermal origins inferred [17–25]. In spite of the development of the equivocal magmatic-hydrothermal model of the ore formation for IOA deposits, the potential REE enrichment in these IOA deposits is still poorly understood. As a unique REE-enriched IOA deposit, the REE mineralization processes in Mushgai Khudag have received limited attention [10].

The structure of apatite gives it the ability to incorporate and concentrate trace elements such as Sr, U, and Th, especially REEs [26]. It is sensitive to geochemical changes in magmatic systems and various fluid-induced chemical and textural changes over a wide range of pressures and temperatures [27–30]. Thus, apatite has been used to trace the petrogenetic processes of magma evolution and hydrothermal alteration [27–30]. In this contribution, we present the in situ U–Pb ages of apatite within magnetite-apatite-enriched rocks and chemical and Sr isotopic compositions of apatite in magnetite-apatite-enriched rocks and syenite as well as calcite in carbonatite together with the bulk rock chemical compositions, aiming to provide insight into the source and genetic history of the Mushgai Khudag complex. The details of the texture and chemical and isotopic compositions of apatite illustrate the constraints of the contribution of the magmatic and hydrothermal

processes to the REE enrichment and mineralization associated with magnetite-apatite-enriched rocks.

2. Geological Background

The Mongolian collage is separated into northern and southern domains by the Main Mongolian Lineament. The Mushgai Khudag alkaline volcanic-plutonic complex is located in the southern domain of Mongolia (Figure 1). The Mushgai Khudag complex is hosted by Paleozoic sedimentary-volcanic sequences and Carboniferous granitoids [10]. It is associated with late Jurassic to early Cretaceous alkaline magmatic activities, including alkaline and subalkaline extrusive, subvolcanic, and intrusive rocks, which range in composition from melanephelinite and nepheline melaleucitite to trachyte in the extrusive facies and shonkinite to syenite in the plutonic facies [8,12]. The alkaline-carbonatite complex is composed of various volcanic and subvolcanic silicate rocks including melanephelinite, theralites, and alkali feldspar trachytes, which are cross-cut by stocks and dykes of alkaline syenites, shonkinites, and magnetite-apatite-enriched rocks, as well as numerous small dykes of carbonatites [10,11]. The complex displays a central ring structure that is almost 30 km in diameter, and the Mushgai Khudag REE deposit is located in the central part of this ring (Figure 2). Twenty ore bodies have been recognized along the endo- and exo-contact parts of syenite and syenite-porphyry [2]. Different ore types have been identified at Mushgai Khudag, including those hosted by carbonatite, mineralized breccia with carbonate cement, magnetite-apatite-enriched rock, and complex phosphate-enriched rocks. A drill core and field investigation showed that carbonatitic and apatite-bearing ores are the two dominant types of REE ore [12]. Carbonatites are ubiquitously associated with fluorite mineralization and contain numerous fluorite veins [13]. The ages of K–Ar in the Mushgai Khudag complex vary widely between 179 and 121 Ma, which might reflect secondary processes [11]. The newly obtained Ar–Ar dating of the magnetite-apatite-enriched rocks and associated silicate rocks (e.g., melanephelinte and alkaline syenite) narrowed the measured age range to 145–133 Ma [13]. The Rb–Sr age of the syenite was shown by Baatar et al. [6] to be 139.9 ± 5.9 Ma.

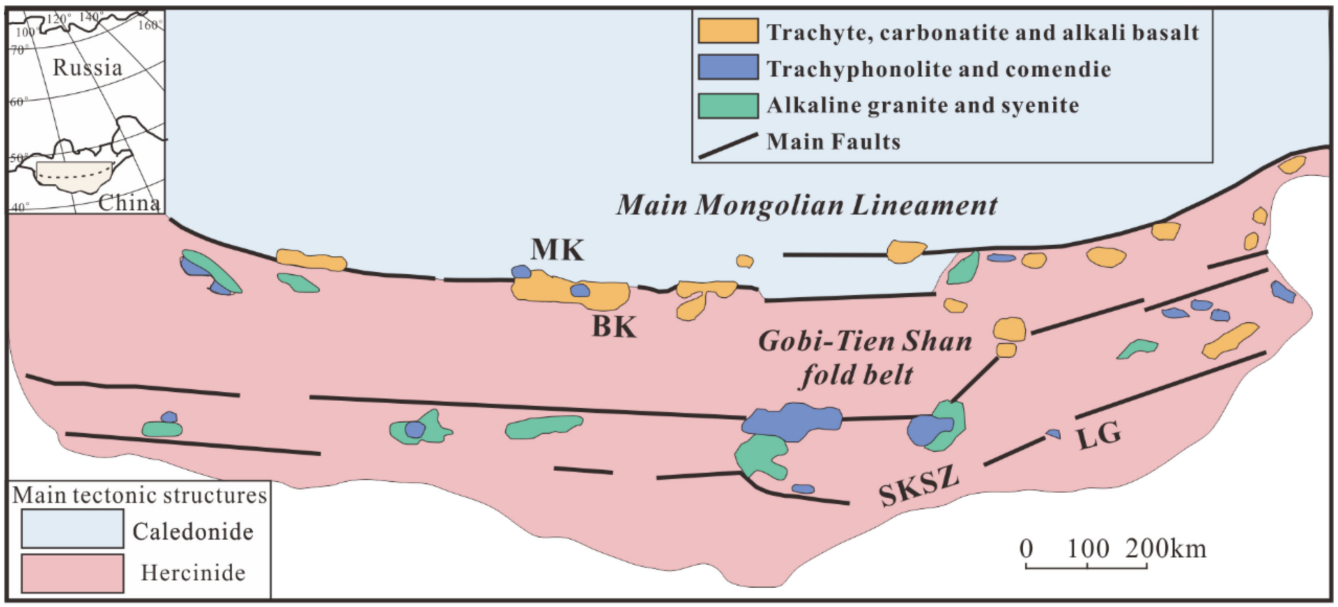

Figure 1. Locations and simplified geological map of the Mushgai Khudag complex modified from Baatar et al. [6]. MK = Mushgai Khudag, BK = Bayan Khoshuu, SKSZ = Sulinkheer suture zone, LG = Lugiin Gol.

Apatite-enriched and magnetite-apatite-enriched rocks are exposed in two stocks of 30 × 70 m and 10 × 30 m in size. The former is known as Apatite Hill and is a typical REE mineralized zone (Figure 2) [10]. Magnetite-dominant rocks occur in the very center,

with apatite dominated rocks on the outside and phlogopite-enriched zones in between. Carbonatite in Apatite Hill occurs as veins and dykes of 0.1 to 10 m in width and is associated with widespread fluorite mineralization. The top of Apatite Hill is usually weathered with britholite and anhydrite. Samples, including fresh and altered magnetite-apatite-enriched rocks, syenites, and carbonatites were collected from Apatite Hill during the 2016 and 2017 HiTech AlkCarb Mongolian Expeditions.

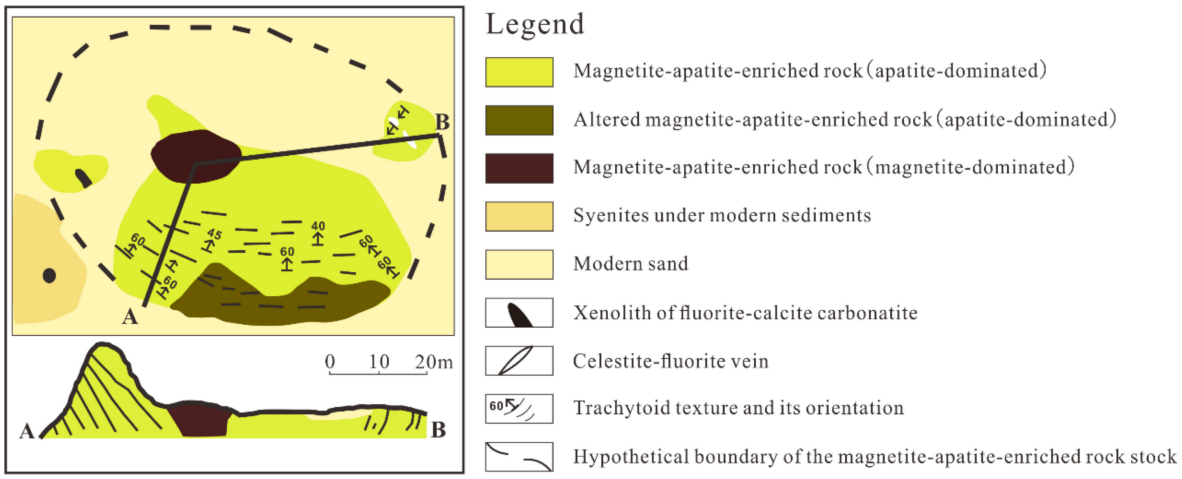

Figure 2. Simplified geological map of magnetite-apatite stock in Mushgai Khudag modified from Nikolenko et al. [10] and Samoilov and Kovalenko [11].

3. Analytical Methods

3.1. Petrographic Analysis

Textures and mineral assemblages of samples prepared in petrographic thin sections were studied using an optical petrographic microscope, an optical microscope coupled with cathodoluminescence (OM-CL), and a scanning electron microscope (SEM) coupled with both energy-dispersive spectrometry (EDS) and back-scattered electron imaging (BSE).

Cathodoluminescence analyses were collected using a Leica DM2700P microscope coupled with a CITL MK5-2 system at the state key laboratory of Geological Processes and Mineral Resources (GPMR), China University of Geosciences (Wuhan). The system was operated at an accelerating voltage of 12 kV and a current density of about 300 μA for calcite and apatite with an exposure time of up to 3s. The CL system was typically operated with a corresponding voltage of 13 kV and a beam current of 400 μA with an exposure time of up to 4 s for feldspar. Back-scattered electron (BSE) images were obtained using a high-definition back-scattered electron detector coupled to a Zeiss Sigma 300 field emission scanning electron microscope (FESEM) at the GPMR. The instrument was operated with a working distance of 8.5 mm, an electronic high tension of 20 kV, and a magnification of 20–100×.

3.2. Chemical Analysis

Major element analyses of whole-rock samples were carried out using a Philips PW 2400 XRF at ALS Minerals-ALS Chemex, Guangzhou. The samples were crushed and powdered in an agate ring mill to pass a 200-mesh sieve. About 1 g of sample was mixed with lithium borate flux ($Li_2B_4O_7$–$LiBO_2$) and fused in an auto fluxer at about 1050 °C to form a flat glass disc for analysis by X-ray fluorescence spectrometry (XRF). Major element compositions were determined with the SARM-4, NCSDC-73510, NCSDC-73303, GBW-7238, and SARM-32 standards with analytical uncertainties of better than 5%. Trace element analyses of whole-rock samples were carried out using an Agilent 7500a ICP-MS at the GPMR. About 50 mg of powdered sample was dissolved with an HF + HNO_3 mixture in high-pressure Teflon capsules. The detailed analytical procedure used for the trace element analyses can be found in Liu et al. [31]. The trace elements were measured together

with the AGV-2, BCR-2, BHVO-2, GSP-2, and RGM-2 standards. The analytical precision was estimated to be better than 10% for all trace elements based on the standards and duplicate analyses.

The major element compositions of apatite were quantified using a JEOL JXA-8230 Electron Probe Microanalyzer equipped with five wavelength-dispersive spectrometers at the Laboratory of Microscopy and Microanalysis, Wuhan Microbeam Analysis Technology Co., Ltd. (Wuhan, China). All thin sections were carbon-coated prior to the analysis. The electron microprobe (EMP) analyses were conducted using an accelerating potential of 15 kV, an incident current of 5 nA, and a spot size of 20 μm. The peak counting time was 10 s for Na, Ca, P, S, Sr, F, Si, Fe, Cl, La, Ce, Pr, Nd, and Sm. The background counting time was half of the peak counting time in the high- and low-energy background positions. The following standards were used: Jadeite (Na), Apatite (Ca, P), Barite (S), Strontium fluoride (Sr), Fluoride (F), Olivine (Si), Pyrope Garnet (Fe), Sodium chloride (Cl), Lanthanum metal (La), Cerium metal (Ce), Praseodymium metal (Pr), Neodymium metal (Nd), and Samarium metal (Sm). The formula of each analyzed spot was calculated based on 25 oxygens as suggested in Ketcham [32].

In situ trace element analyses for calcite and apatite were conducted using a RESOlution 193 nm laser ablation system coupled to a Thermo iCAP-Q Inductively Coupled Plasma Mass Spectrometer (ICP-MS) at the GPMR. The NIST SRM 612 international glass standard was used to correct the instrument drift, and USGS reference glasses (BIR-1G, BCR-2G, and BHVO-2G) were adopted as external standards for concentration calibration [33]. Standards and samples were analyzed with a 33 μm spot size, a 10 Hz repetition rate, and a corresponding energy density of approximately 5–7 J/cm^2. Each spot analysis incorporated 30 s of background acquisition and 40 s of sample data acquisition. Elements of data reduction, including the concentration determination, detection limit, and individual run uncertainty were calculated using ICPMSDataCal software [33]. The analytical uncertainty for most trace elements in calcite and apatite was within 10% and was better than 5% for REEs.

3.3. In Situ U–Pb Dating of Apatite

In situ U–Pb dating of apatite was carried out using the RESOlution laser ablation coupled to the iCap-Q ICP-MS at the GPMR. The details of the analytical procedure and the method of correction used for the common Pb component can be found in Chen and Simonetti [34]. Madagascar apatite (MAD) was utilized as an external standard to monitor instrumental drift and U/Pb fractionation [35]. Standards and samples were ablated using a spot size of 50 μm, a repetition rate of 8 Hz, and an energy density of 5–7 J/cm^2. Each spot analysis incorporated 30 s of background acquisition and 40 s of sample data acquisition. The data calculation was carried out using an Excel-based program developed by Chen and Simonetti [34]. Tera–Wasserburg diagrams and weighted mean $^{206}Pb/^{238}U$ ages were constructed using Isoplot v3.0 [36].

3.4. In Situ Sr Isotope Determinations

In situ Sr isotope analyses for apatite and calcite were conducted using the RESOlution laser ablation system coupled to the Nu Plasma II multi-collector (MC) ICP-MS at the GPMR. The measurements involved correction of spectral interference for Kr, Rb, and doubly-charged REE, as described by Chen and Simonetti [37]. Analyses of calcite and apatite were carried out using a spot size of 50 μm, a repetition rate of 10 Hz, and an energy density of approximately 5–7 J/cm^2. An in-lab coral standard (Qingdao) was analyzed as the external standard to evaluate the reliability of analytical accuracy. The average $^{87}Sr/^{86}Sr$ isotopic composition obtained for the coral standard was 0.70917 ± 0.00004 (2σ, n = 24), which is consistent with the recommended value of 0.70923 ± 0.00002, as determined by ID-TIMS at the State Key Laboratory for Mineral Deposits Research at Nanjing University [38].

4. Petrography

4.1. Magnetite-Apatite-Enriched Rocks and the Dominant Apatite

Paragenesis and textural details for apatite from magnetite-apatite-enriched rocks are presented in Figure 3. Some of the magnetite-apatite-enriched rocks show obvious alterations. The fresh magnetite-apatite-enriched rocks are commonly yellow-green to pale green and porphyritic in texture, with apatite phenocryst accounting for 90 vol.% (Figure 3a). Euhedral to subeuhedral magmatic apatite is commonly identified in these rocks, with grain sizes varying from 100 μm to 10 mm (Figure 4b–d). Coarse-grained apatite (Ap-1) displays heterogeneous purple luminescence with dispersed yellowish zones, accompanied by minor fissures characterized by orange luminescence (Figure 3b). Fine-grained apatite (Ap-2), commonly 100–500 μm in grain size, shows an internal structure characterized by a darker core and a lighter rim on the BSE images (Figure 3c). Some fine-grained apatite occurs as aggregates with phosphosiderite filled in the fissures (Figure 3d). The groundmass primarily consists of celestine and phosphosiderite, accompanied by minor concentrations of magnetite, monazite, fluorite, and quartz (Figure 3c). Anhedral fine-grained celestine (10–200 μm) makes up approximately 80 vol.% of the groundmass, with the rest dominated by phosphosiderite that generally occurs along the grain boundaries of apatite (Figure 3c,d). Small secondary monazite crystals that are 1–2 μm in grain size, accounting for less than 1 vol.%, occur in association with phosphosiderite in the groundmass (Figure 3c).

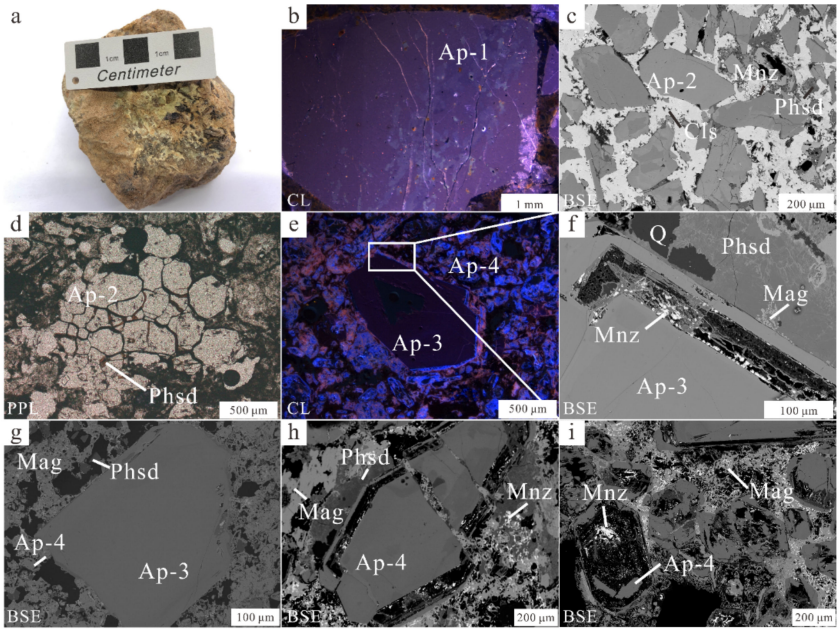

Figure 3. Transmitted plane-polarized light, cathodoluminescence, and back-scattered electron photomicrographs illustrating the key petrographic features of magnetite-apatite-enriched rocks and the dominant apatite. (**a**) Hand specimen of the yellowish magnetite-apatite-enriched rocks; (**b**) coarse-grained magmatic apatite (Ap-1) displaying heterogeneous purple luminescence with dispersed yellow luminescent zones; (**c**) fine-grained magmatic apatite (Ap-2) associated with anhedral fine-grained celestine (Cls), phosphosiderite (Phsd), and minor monazite (Mnz); (**d**) fine-grained magmatic apatite aggregates with phosphosiderite occurring along the grain boundaries; (**e**) coarse-grained slightly altered apatite (Ap-3) showing dark purple luminescence associated with fine-grained altered apatite (Ap-4) illustrating various levels of blue-purple luminescence; (**f**) fine-grained monazite crystals deposited in the fissures along a slightly altered apatite (Ap-3) rim associated with phosphosiderite, magnetite (Mag), and a minor concentration of quartz (Q); (**g**) Ap-3 showing a thin darker rim on the BSE images; (**h**) fractured Ap-4 with magnetite, phosphosiderite, and secondary monazite precipitated in the fissures or along the boundaries; (**i**) fine-grained monazite aggregates crystallized in the Ap-4 hollows and along the boundaries associated with hydrothermal magnetite.

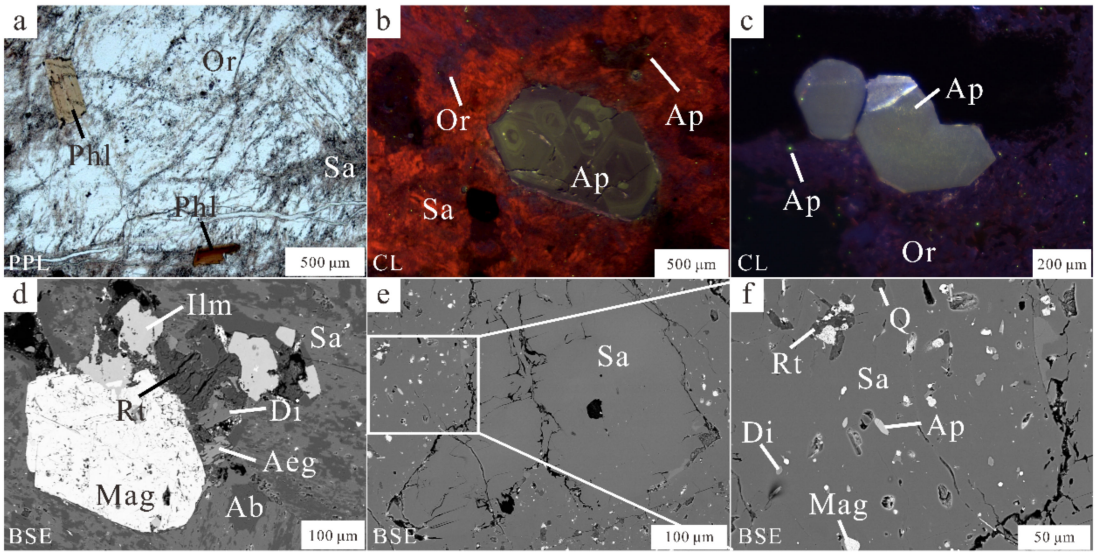

Figure 4. Transmitted plane-polarized light, cathodoluminescence, and back-scattered electron photomicrographs illustrating the key petrographic features of syenite and apatite. (**a**) Coarse-grained orthoclase (Or), phlogopite (Phl), and sanidine (Sa) phenocryst in syenite; (**b**) prismatic magmatic apatite displaying oscillatory zoning with various levels of purple to yellow luminescence and sanidine showing a red CL color; (**c**) irregular apatite showing relatively uniform yellow luminescence; (**d**) minor phlogopite, apatite, quartz, magnetite, ilmenite (Ilm), rutile (Rt), aegirine (Aeg), and diopside (Di) in the groundmass; (**e**,**f**) tiny acicular apatite disseminated in quartz, magnetite, ilmenite, rutile, and aegirine.

The altered magnetite-apatite-enriched rocks are gray to earthy yellow with a porphyritic structure, and apatite phenocryst accounts for 80 vol.% associated with minor magnetite, monazite, fluorite, phosphosiderite, and celestine (Figure 3e,g). Coarse-grained apatite (Ap-3) with slight alterations occurs as disseminated crystals in the more abundant fine-grained apatite (Ap-4) with strong alterations in the altered magnetite-apatite-enriched rocks. Ap-3 displays dark purple luminescence and is 500–2000 μm in size. Some Ap-3 shows alterations with fine-grained monazite crystals (<10 μm) precipitated in the fissures along the crystal rims (Figure 3e,f), whereas others are relatively euhedral with limited alterations (Figure 3g). Ap-4 displays various levels of blue to purple luminescence with grain sizes of 50–1000 μm and is strongly fractured with fissures in the rim or altered as hollows with small relict apatite mostly distributed along the rim. Fine-grained magnetite and monazite occur in the altered fissures and hollows (Figure 3h,i). The monazite grains or aggregates in the altered zones, accounting for 3–5 vol.%, are secondary in nature. The abundance of magnetite, monazite, and fluorite in the altered magnetite-apatite-enriched rocks is greater than in fresh rocks, whereas the distributions of phosphosiderite and celestine have sharply declined (Figure 3).

4.2. Syenite and Apatite

The paragenesis and texture of apatite from syenite are shown in Figure 4. Mushgai Khudag syenite contains variable amounts of orthoclase and sanidine with minor concentrations of phlogopite, apatite, quartz, magnetite, ilmenite, rutile, and titanite (Figure 4a–d). Orthoclase with grain sizes of up to 1–10 mm is characterized by blue luminescence, whereas sanidine with grain sizes of 100–500 μm displays a red CL color (Figure 4a,b). Most apatite within syenite appears to be euhedral, which is prismatic and 200 to 500 μm in size (Figure 4b). Oscillatory zoning within the prismatic grains is evident in CL images, ranging from purple to yellow in color (Figure 4b). A small number of ovoid or irregular apatite grains display relatively uniform yellow luminescence (Figure 4c). Acicular apatite with grain sizes of 1–10 μm can be identified as being disseminated within quartz, aegirine, and ilmenite (Figure 4e,f). It displays a green CL color with aspect ratios ranging from 5 to 10.

4.3. Carbonatite and the Dominant Calcite

The paragenesis and textural details for calcite and minor minerals from carbonatite are shown in Figure 5. Carbonatite is brown or yellowish-gray in color and mainly consists of calcite, fluorite, celestine, and barite with accessory quartz and REE minerals (e.g., bastnaesite and parasite). Calcite accounts for 70 vol.% with variable grain sizes ranging from 20 μm to 2 mm. Coarse-grained calcite (1–2 mm) appears relatively subeuhedral with jagged grain boundaries, suggesting the occurrence of hydrothermal overprinting (Figure 5a). Fine-grained calcite (20–50 μm) is anhedral and is commonly found to surround the coarse-grained calcite (Figure 5a). Fluorite, accounting for 15 vol.%, varies from 10 μm to 2 mm in grain size (Figure 5a,b). Celestine is anhedral with grain sizes of 10 to 20 μm, and it is widely disseminated in carbonatite, making up 5 vol.% (Figure 5c). Barite occurs as very fine-grained crystals smaller than 20 μm in size and is commonly associated with quartz and REE minerals (e.g., bastnaesite and parasite; Figure 5d,e). The parasite shows zonation in the BSE images due to variable levels of REE abundance, and it commonly occurs in association with celestine as inclusions in calcite (Figure 5e,f).

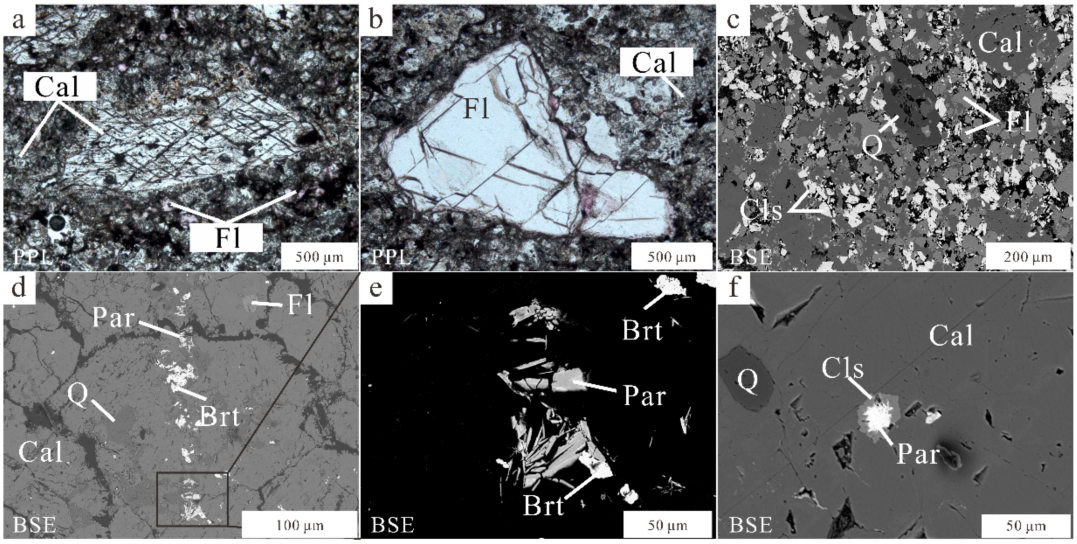

Figure 5. Transmitted plane-polarized light and back-scattered electron photomicrographs illustrating the key petrographic features of carbonatite and calcite. (**a**) Euhedral coarse-grained calcite (Cal) with jagged grain boundaries associated with fine-grained calcite and purple fluorite (Fl); (**b**) coarse-grained fluorite associated with fine-grained calcite; (**c**) calcite, fluorite, celestine (Cls) with accessory quartz; (**d**,**e**) barite (Brt) associated with quartz and parasite (Par) disseminated in calcite; (**f**) parasite together with celestine occurring as inclusions in calcite.

5. Results

5.1. Major and Trace Element Compositions for Magnetite-Apatite-Enriched Rocks, Syenites, and Carbonatites

The major and trace element compositions of magnetite-apatite-enriched rocks, syenites, and carbonatites are listed in Table S1. Fresh and altered magnetite-apatite-enriched rocks show variations in concentrations of major elements, especially Fe_2O_3, SO_3, and SiO_2. The contents of Fe_2O_3 (1.50–2.75 wt.%) and SO_3 (1.32–2.34 wt.%) in the fresh magnetite-apatite-enriched rocks are lower than in the altered rocks (15.62–23.88 wt.% and 3.57–5.89 wt.%, respectively). The SiO_2 content of the former (7.38–8.48 wt.%) is higher than that of the latter (2.35–5.16 wt.%). As illustrated in the primitive mantle normalized trace element plots (Figure 6a), the Mushgai Khudag magnetite-apatite-enriched rocks are characterized by significant enrichments of REE and U and depletion of HFSE (e.g., Nb, Ta, Zr, and Hf). In addition, the patterns show obvious negative Sr and Pb anomalies, which are consistent with data previously reported by Nikolenko et al. [13]. Magnetite-apatite-enriched rocks display strong REE enrichment (21,929–49,660 ppm) compared with the

typical magnetite-apatite-enriched rocks found elsewhere in the world (e.g., approximately 120 ppm in the Los Colorados IOA, Chile) [24]. Of note, the altered magnetite-apatite-enriched rocks have distinctly higher REE concentrations (58,036 ± 13,313 ppm) than the fresh magnetite-apatite-enriched rocks (28,681 ± 6752 ppm), a characteristic that was also observed by Nikolenko et al. [10]. Nb/Ta and Zr/Hf values show large variations for both fresh and altered samples, ranging from 22.1 to 35.0 and 37.2 to 127, respectively. The chondrite-normalized REE patterns of magnetite-apatite-enriched rocks are steep and show significant LREE enrichments with $(La/Yb)_N$ ranging from 85 to 257 (Figure 6b). The $(La/Yb)_N$ of the altered magnetite apatite-enriched rocks (225 ± 33) is higher than that of the fresh rocks (117 ± 32) as well.

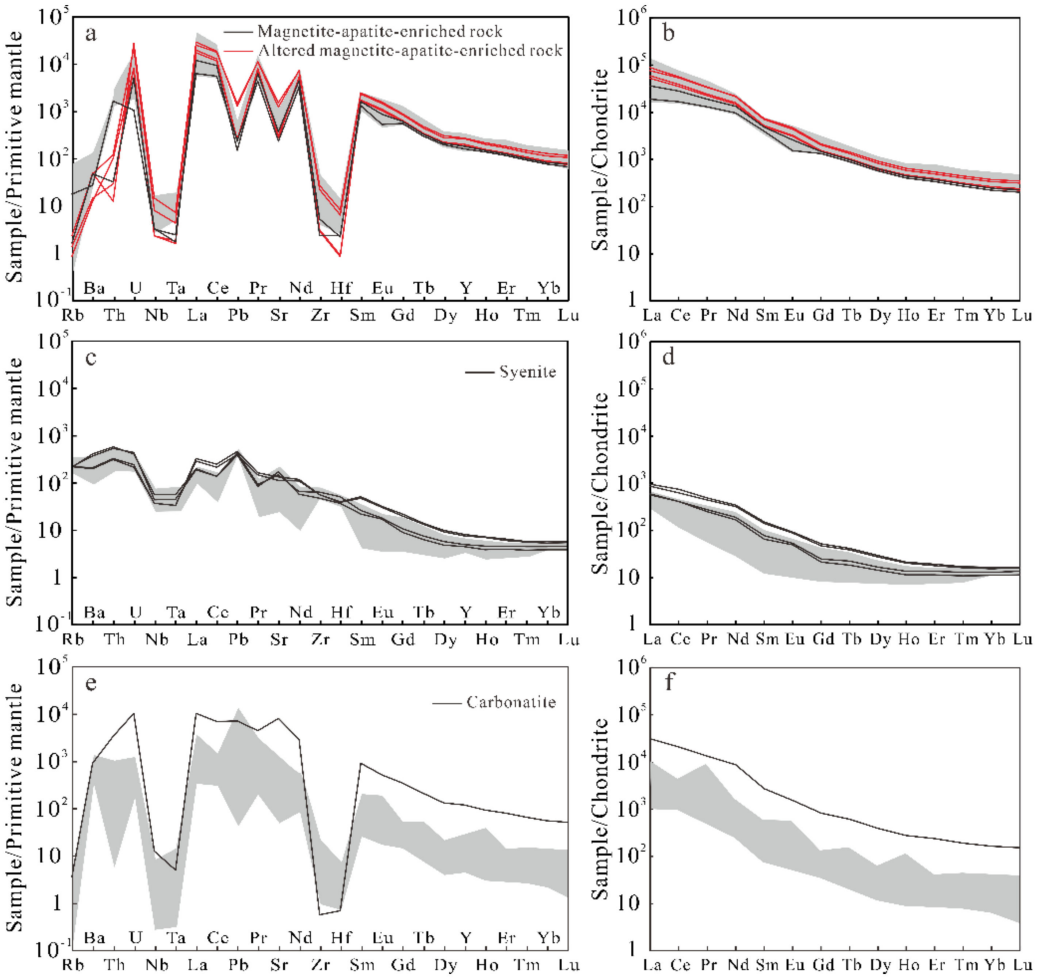

Figure 6. Primitive mantle normalized trace element and chondrite-normalized REE patterns of magnetite-apatite-enriched rocks (**a**,**b**), syenites (**c**,**d**), and carbonatites (**e**,**f**) from the Mushgai Khudag complex. Normalization values were adopted from McDonough and Sun [39] and Sun and McDonough [40], respectively. Reported data for these rocks are presented as grey shades for comparison [6,10,13].

Syenites contain 63.16–63.27 wt.% of SiO_2 and 11.80–11.56 wt.% of $Na_2O + K_2O$ and are plotted in the syenite field of the TAS (Total Alkali and Silica) diagram (Table S1) [41]. The primitive mantle normalized trace element patterns obtained are similar to those reported by Nikolenko et al. [13], showing positive Pb and Sr anomalies and negative Nb and Ta anomalies (Figure 6c). The chondrite-normalized REE patterns of syenite show LREE enrichment (Figure 6d). Syenites display much lower and limited variation in REE contents (519–956 ppm) and $(La/Yb)_N$ values (46.1–52.5) compared with magnetite-apatite-enriched rocks.

The CaO/(CaO + MgO + FeO + MnO) value of carbonatite is 0.95, which can be classified as calciocarbonatite [42]. Mushgai Khudag carbonatite shows significant enrichment in REE (26,692 ppm), U (229 ppm), Th (259 ppm), and Sr (177,066 ppm) and depletion in HFSE (<10 ppm), which is generally similar to the composition of carbonatites worldwide [43,44]. Obvious positive Pb and Sr anomalies are displayed in the primitive mantle normalized diagrams (Figure 6e). Carbonatites show chondrite-normalized REE patterns that are highly enriched in LREEs (La/Yb_N = 191) (Figure 6f). The carbonatite samples are more enriched in trace elements including REEs compared to the results reported by Baatar et al. [6] and Nikolenko et al. [13], which suggests heterogeneous chemical distributions for different carbonatite dykes at Mushgai Khudag.

5.2. Mineral Compositions for Apatite within Magnetite-Apatite-Enriched Rocks and Syenites

The major and trace element compositions for magmatic and altered apatite from magnetite-apatite-enriched rocks and syenites were determined using an electron microprobe and LA-ICP-MS, respectively, and are listed in Table S2.

All apatite from Mushgai Khudag corresponds to fluorapatite with F contents of 2.73 to 3.77 wt.%. Apatite from magnetite-apatite-enriched rocks is characterized by high contents of SiO_2, SO_3, and $LREE_2O_3$ (0.36–5.59 wt.%, 0.86–4.17 wt.%, and 2.62–9.22 wt.%, respectively) compared to those within the typical magnetite-apatite-enriched rocks (SiO_2 < 0.92 wt.%, SO_3 < 2.93 wt.%, and $LREE_2O_3$ < 0.59 wt.%) [25]. Altered apatite shows higher contents of SiO_2 (up to 5.59 wt.%), SO_3 (up to 4.17 wt.%), and $LREE_2O_3$ (up to 9.22 wt.%) than magmatic apatite (0.94 wt.%, 1.40 wt.% and 4.39 wt.% on average, respectively; Figure 7). Slightly altered apatite also contains higher concentrations of SiO_2 and $LREE_2O_3$ but shows a comparable SO_3 concentration compared with magmatic apatite (Figure 7). An increased LREE content in apatite correlates with an increased Si abundance, which suggests a coupled substitution scheme of $Si^{4+} + REE^{3+} = P^{5+} + Ca^{2+}$ (Figure 7a) [26]. The LREE and Si contents of slightly altered apatite (Ap-3) have the same substitution trend as magmatic apatite (Ap-1 and Ap-2) (Figure 7a). Of note, altered apatite (Ap-4) also displays correlated increases in S and LREE contents (Figure 7b). This suggests that the $S^{6+} + REE^{3+} = P^{5+} + 2Ca^{2+}$ substitution scheme also contributes to REE incorporation into the apatite structure of Ap-4 in addition to the coupled Si substitution scheme [26].

Apatite from magnetite-apatite-enriched rocks and syenites is characterized by enrichment with REE, Th, and U and depletion of HFSE (e.g., Nb, Ta, Zr, Hf). Interestingly, the REE content within apatite shows positive correlations with U, V, and Zr (Figure 8a). Chondrite-normalized REE patterns for Mushgai Khudag apatite are characterized by significant LREE enrichment (46,066 ± 71,391 ppm) with high $(La/Yb)_N$ values (176 ± 103) (Table S2; Figure 9a–c). The REE contents and $(La/Yb)_N$ ratios for different types of apatite show variations. Altered and slightly altered apatite within the altered magnetite-apatite-enriched rocks contain the highest levels of REE abundance (65,988 ± 56,322 ppm) and $(La/Yb)_N$ values (237 ± 71), whereas apatite within syenite is the most depleted in terms of the REE abundance (14,741–30,220 ppm; Table S2). Magmatic apatite (Ap-1 and Ap-2) generally displays a lower REE content (39,414 ± 47,876 ppm) and $(La/Yb)_N$ ratio (237 ± 71) compared with altered apatite (Ap-4; 63,912 ± 31,785 ppm and 241 ± 40, respectively). Nb/Ta, Zr/Hf, Eu/Eu*, Y/Ho, and $(La/Sm)_N$ ratios for magmatic and altered apatite also show significant differences (Table S2; Figure 8b–d). Magmatic apatite is characterized by lower Nb/Ta and Zr/Hf ratios than altered apatite. Altered apatite generally lacks Eu anomalies (Eu/Eu* = 0.857–0.964), whereas magmatic apatite shows slight negative Eu anomalies with a variable Eu/Eu* ranging from 0.608 to 0.799. Y/Ho values for magmatic apatite show limited variation of 30–33, whereas those for altered apatite are mostly larger than 34 (Figure 8d).

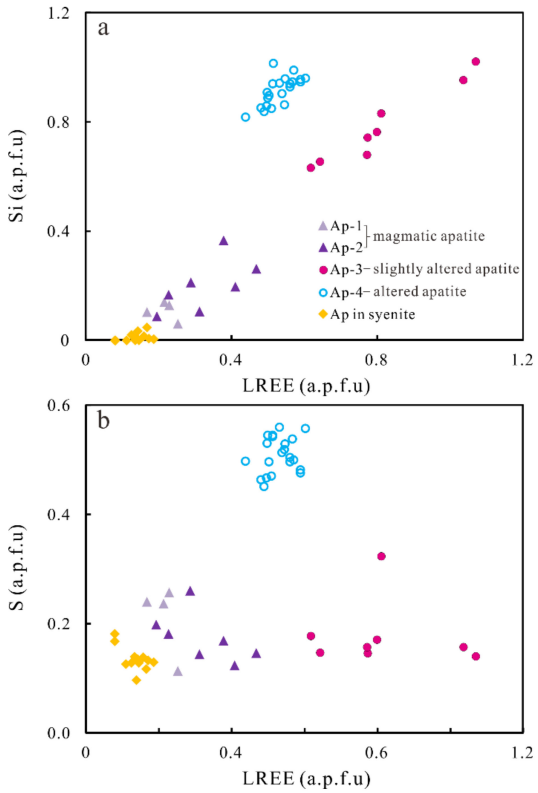

Figure 7. Major element compositions of apatite within magnetite-apatite-enriched rocks and syenites. (**a**) The plot illustrates the correlated increases in LREE and Si in apatite; (**b**) the plot shows the relatively consistent S content in magmatic and slightly altered apatite (Ap-1, Ap-2 and Ap-3) and the correlated increases in S and LREE contents for altered apatite (Ap-4).

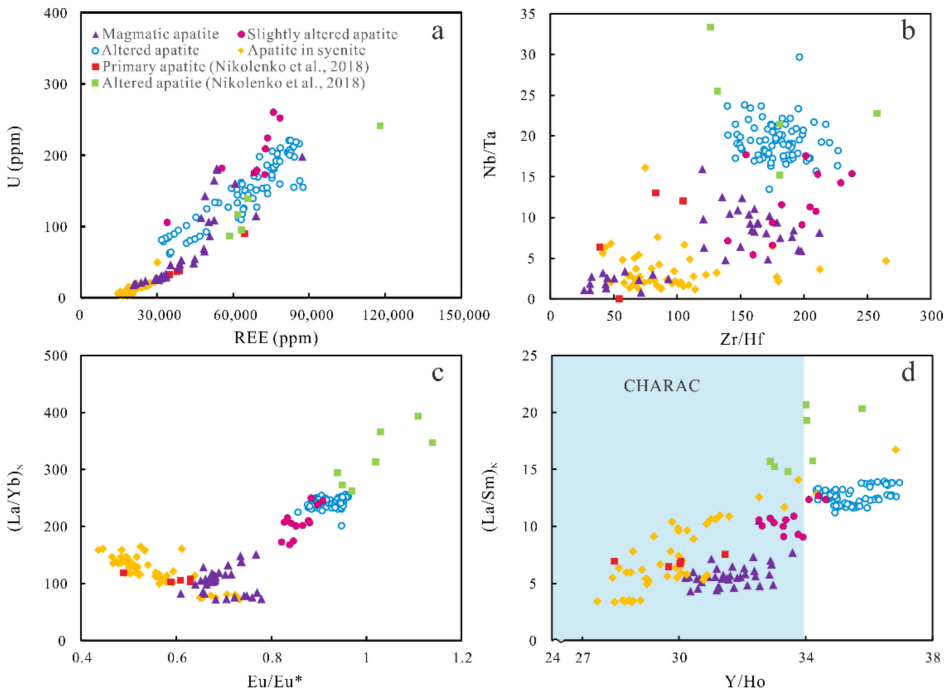

Figure 8. Diagrams displaying trace-element variations of apatite within magnetite-apatite-enriched rocks and syenites from Mushgai Khudag. (**a**) ΣREE versus U; (**b**) Zr/Hf versus Nb/Ta; (**c**) Eu/Eu* versus La/Yb_N; (**d**) Y/Ho versus La/Sm_N. The CHArge-and-RAdius-Controlled (CHARAC) interval of Y/Ho ratios in (**d**) was taken from Bau [45].

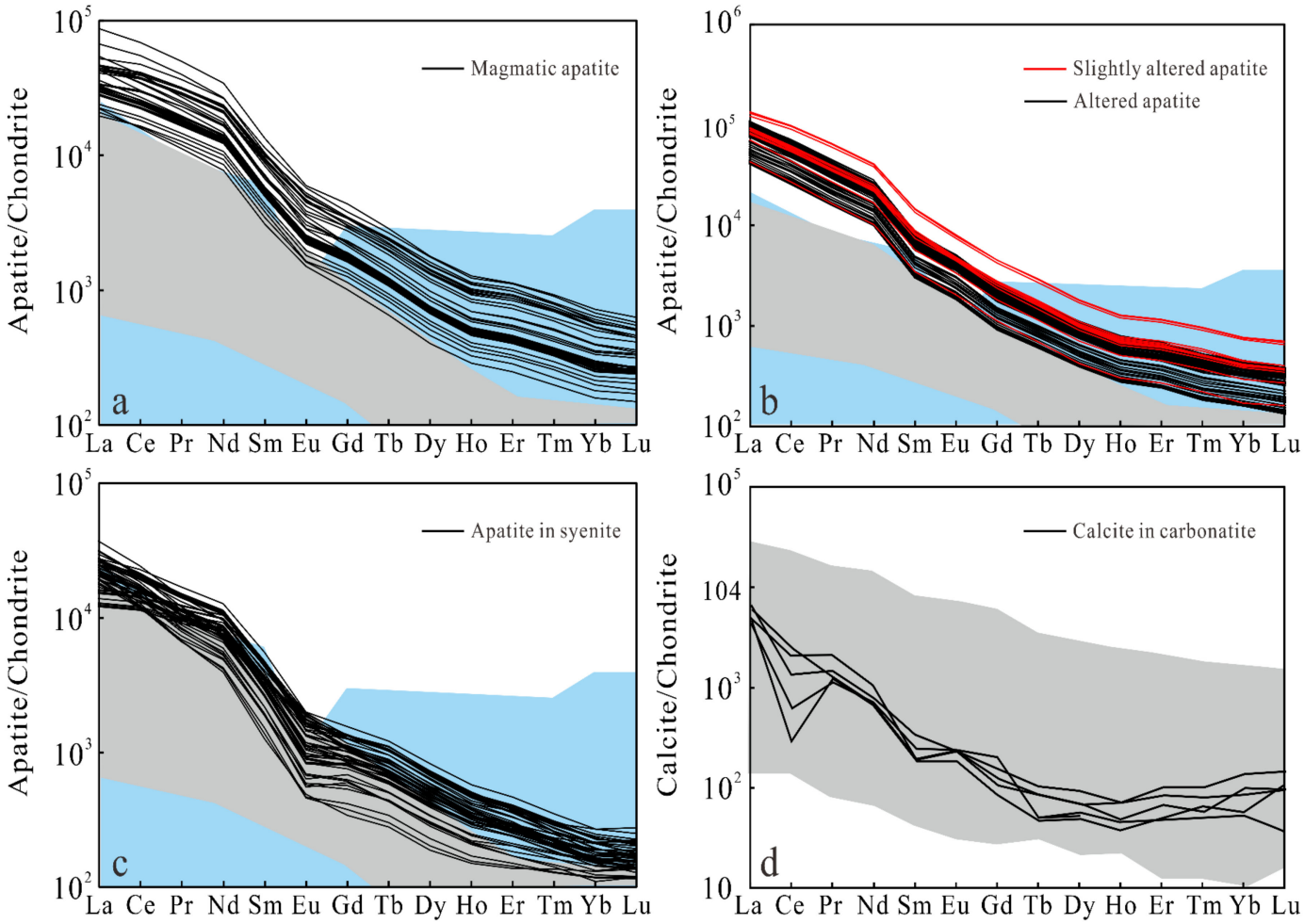

Figure 9. Chondrite-normalized REE patterns of apatite from magnetite-apatite-enriched rocks and syenites (**a**–**c**) and calcite from carbonatite (**d**). Normalization values were adopted from Sun and McDonough [40]. Previously reported apatite data from magnetite-apatite-enriched rocks and carbonatite are presented in blue and gray in (**a**–**c**) for comparison [25,27,34,43,44], and calcite data from carbonatite are presented in gray in (**d**) for comparison [27,34,46–49].

Apatite with different levels of cathodoluminescence mostly shows variation in the REE content. Magmatic apatite from magnetite-apatite-enriched rocks shows light to dark purple luminescence, which is related to the variable content of Ce^{3+} [50]. Dark purple apatite grains are characterized by higher Ce contents (up to 60,304 ppm) compared with the light purple ones (as low as 9748 ppm) (Figure 10a,b). Oscillatory-zoned apatite from syenite displays variable yellow to purple zones in the CL images (Figure 10c). From core to rim, the abundance of REE, Zr, U, and Th varies in the ranges of 17,268–27,521, 9.19–23.1, 8.83–21.9, and 67.2–313 ppm, respectively (Table S2). The oscillatory geochemical variation correlates well with the zonation identified with CL (Figure 10c,d). The purple zone is characterized by enriched REE, Zr, U, and Th, whereas the light-yellow zone is relatively depleted in these elements (Figure 10c,d). Both $(La/Yb)_N$ and $(La/Nd)_N$ decrease in the core and increase in the rim, changes that are decoupled from the oscillatory variation (Figure 10e,f).

5.3. Mineral Compositions for Dominant Calcite in Carbonatite

The trace element compositions for calcite from carbonatite are listed in Table S3. Calcite from the Mushgai Khudag carbonatite shows strong enrichment of REE, Sr, Ba, and Pb and depletion of HFSE (e.g., Nb, Ta, Zr, Hf), similar to calcite from carbonatites worldwide (Table S3). Of note, Pb is enriched in calcite from Mushgai Khudag in concentrations

varying from 6.59 to 416 ppm (Table S3). Chondrite-normalized REE patterns for Mushgai Khudag calcite show strong LREE enrichment (183–337 ppm) with relative HREE depletion (5.90–10.6ppm) (Table S3; Figure 9d). The LREE-enriched trend is a typical characteristic of primary calcite in carbonatites worldwide, such as in Oka carbonatite (Figure 9d) [34]. $(La/Yb)_N$ ratios of calcite vary from 38.4 to 101 with the majority being between 50 and 100 (Table S3). Some calcite displays a significant negative Ce anomaly ($Ce/Ce^* = 0.41 \pm 0.29$; Figure 9d).

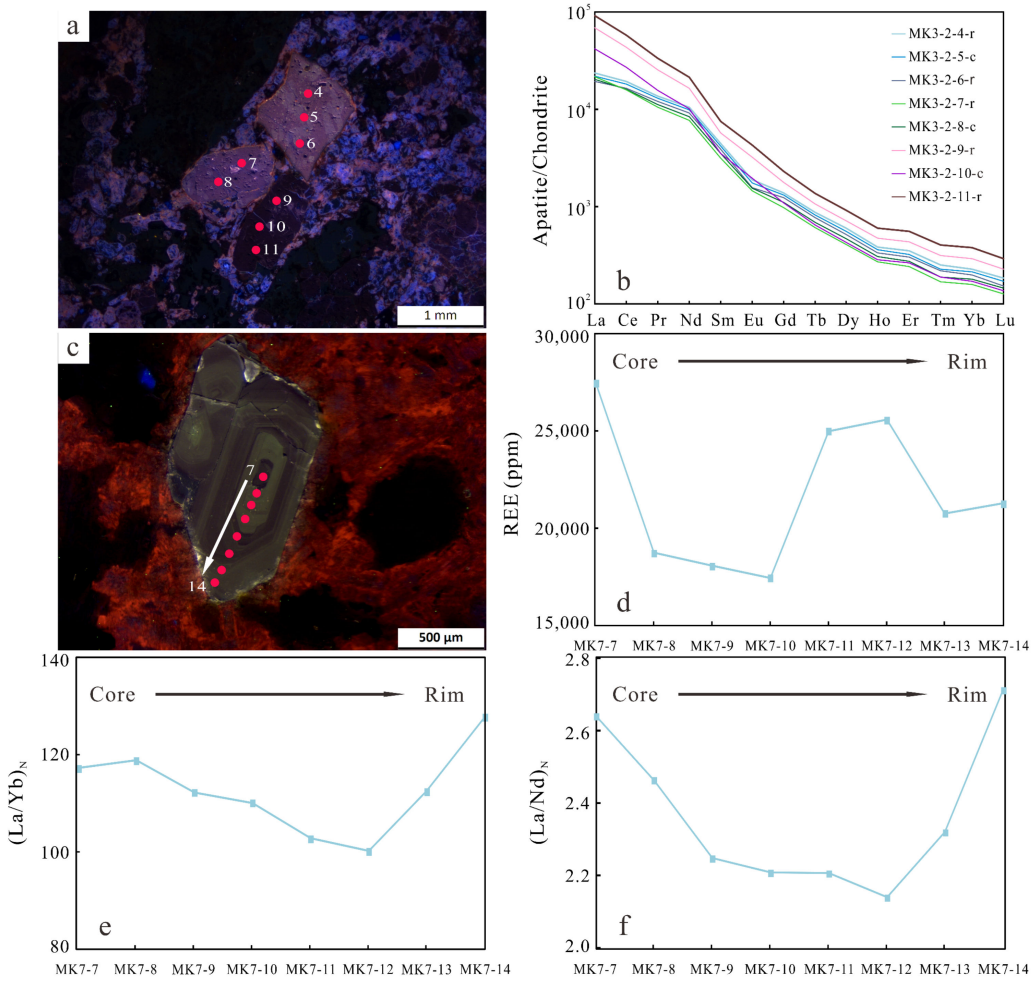

Figure 10. Apatite from magnetite-apatite-enriched rocks and syenites displaying trace-element variations. (**a**,**b**) Dark purple luminescent apatite grains characterized by higher REE contents than the light purple luminescent ones; (**c**–**f**) trace element composition variation trends recording the oscillatory zonation of apatite within syenite. The red dots and the accompanying number (**a**,**c**) refer to the analytical points of samples. 4–11 in (**a**) refer to MK3-2-4 to MK3-2-11 in (**b**); 7, 14 in (**c**) refer to MK7-7 and MK7-14 in (**d**–**f**).

5.4. U–Pb Ages of Apatite within the Magnetite-Apatite-Enriched Rocks

Trace element data suggest that both magmatic and altered apatite are characterized by a high U content ranging from 17.4 to 512 ppm, which favors high-quality U–Pb dating (Table S3). U–Pb geochronological data for magmatic apatite (Ap-1 and Ap-2) and altered apatite (Ap-4) from magnetite-apatite-enriched rocks are listed in Table S4 and shown in Figure 11. Both magmatic and altered apatite were dated in situ by LA-ICP-MS and similar U-Pb ages of 140.7 ± 5.4 and 138.0 ± 5.1 Ma were found, as shown in the Tera–Wasserburg plots (Figure 11a,b). The y-intercept corresponds to a $^{207}Pb/^{206}Pb$ ratio that represents the best estimate for the composition of the common Pb component. The common Pb corrected weighted mean $^{206}Pb/^{238}U$ ages are 139.7 ± 2.6 and 138.0 ± 1.3 Ma,

respectively (Figure 11c,d), which is consistent with the Rb–Sr age in the associated syenite (139.9 ± 5.9 Ma) [6].

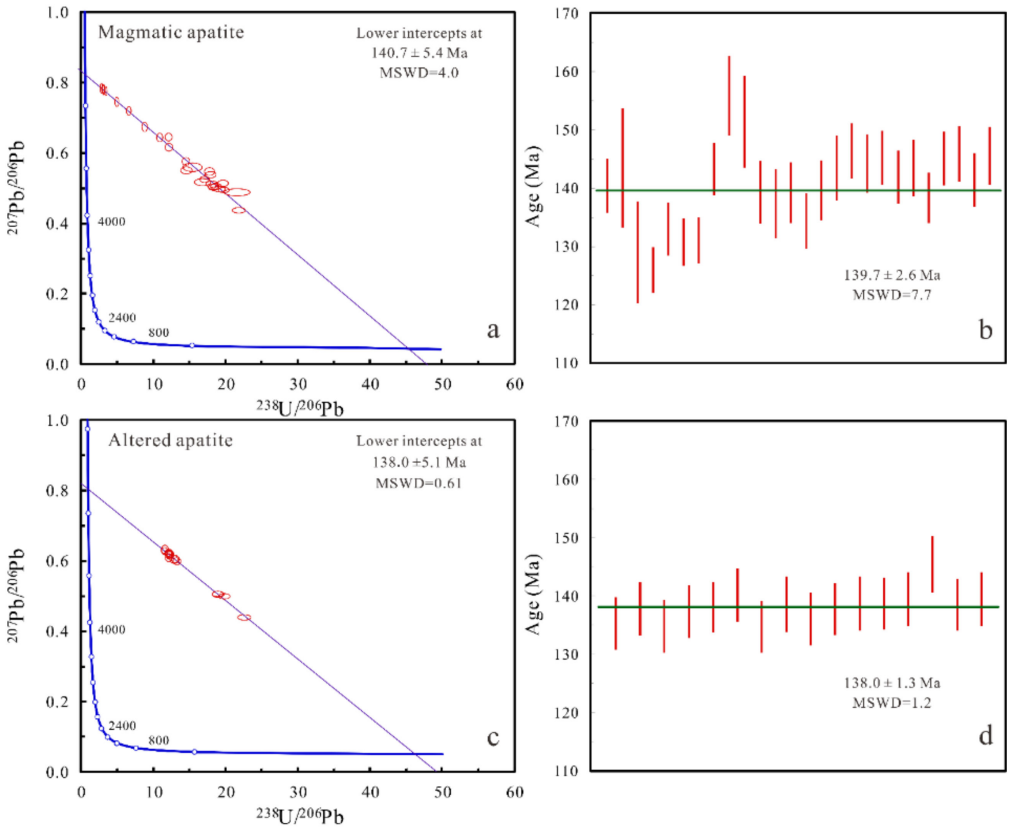

Figure 11. Tera–Wasserburg plots and weighted mean $^{206}Pb/^{238}U$ age diagrams for magmatic and altered apatite within magnetite-apatite-enriched rocks.

5.5. In Situ Sr Isotopic Compositions

The Rb/Sr ratios for both calcite and apatite are extremely low (less than 0.001; Table S3); therefore, the measured $^{87}Sr/^{86}Sr$ ratios obtained for individual grains can be considered to be their initial Sr isotopic compositions due to the negligible radiogenic contribution of ^{87}Sr. In situ Sr, isotopic compositions of apatite from magnetite-apatite-enriched rocks and syenite and calcite from carbonatite are reported in Table S5 and presented in Figure 12. The Sr isotopic compositions of magmatic apatite (Ap-1 and Ap-2) show narrow variations as well as slightly altered and altered apatite (Ap-3 and Ap-4) with $^{87}Sr/^{86}Sr$ ratios of 0.70598–0.70626 and 0.70590–0.70648, respectively. Apatite from syenite also shows relatively consistent Sr isotopic compositions with $^{87}Sr/^{86}Sr$ ratios of 0.70572–0.70619. Thus, the different apatite samples exhibit a limited range of $^{87}Sr/^{86}Sr$ values with an average of 0.70606 (Table S5; Figure 12a). In addition, calcite from carbonatite shows a similar level of $^{87}Sr/^{86}Sr$ variation (0.70619–0.70641) compared with apatite from magnetite-apatite-enriched rocks and syenites (Table S5; Figure 12b).

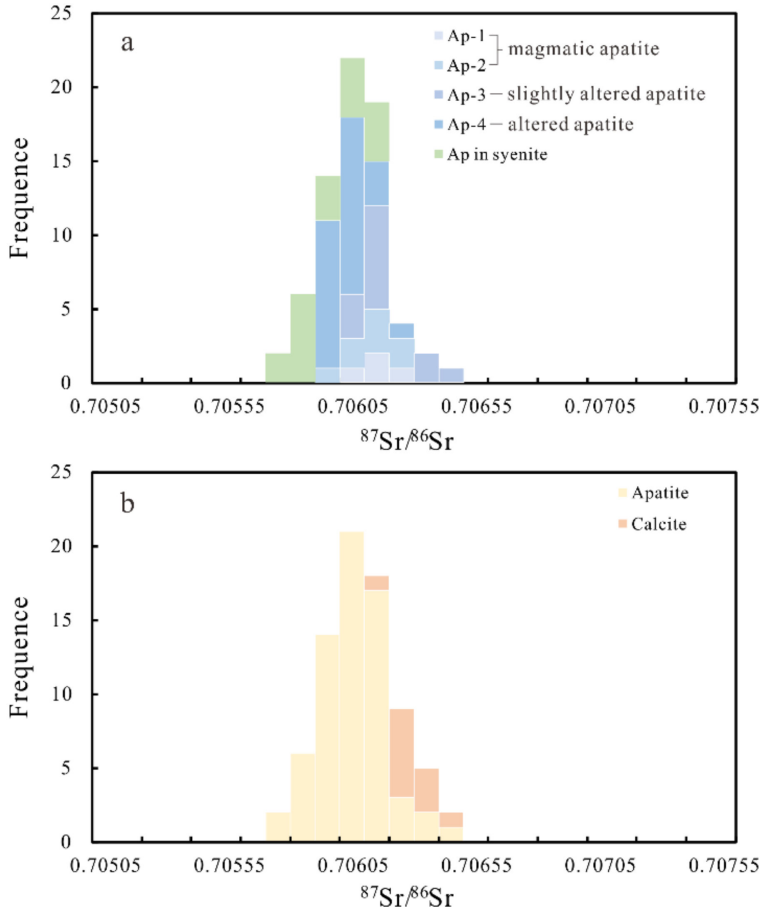

Figure 12. In-situ Sr isotopic compositions of apatite from magnetite-apatite-enriched rock and syenite (**a**) and calcite from carbonatite (**b**).

6. Discussion

6.1. Age and Sources of the Mushgai Khudag Complex

The newly obtained $^{206}Pb/^{238}U$ age of 139.7 ± 2.6 Ma for apatite within magnetite-apatite-enriched rocks is consistent with the Rb–Sr age of the associated syenite (139.9 ± 5.9 Ma) and is in good agreement with the Ar–Ar dating age range (145–133 Ma) [6,13]. Magnetite-apatite-enriched rocks are considered to be the products of silicate–salt liquid immiscibility from the highly evolved parental alkaline silicate melt based on the melt and fluid inclusion data presented by Andreeva and Kovalenko [9] and Nikolenko et al. [10]. The newly obtained U–Pb ages, which are consistent with alkaline silicate rocks and carbonatite, strongly support the liquid immiscibility model. The Rb–Sr age of syenite (130.6 ± 9.3 Ma) in the Bayan Khoshuu complex, which is not far from the Mushgai Khudag complex, is also similar to the obtained ages for the Mushgai Khudag complex [6]. Other carbonatite complexes in Central Asia include Ulgii Khiid and those in West Transbaikalia and Central Tyva in Russian Siberia [6,11,51]. The age obtained for the Ulgii Khiid complex was 147–158 Ma, and carbonatites and associated alkaline silicate rocks from Western Transbaikalia and Central Tyva yielded ages of 131–118 and 118–117 Ma, respectively [11,52–54]. The similarity in ages (Early Cretaceous) supports the presence of late Mesozoic regional alkaline-carbonatite magmatism in Central Asia, which is attributed to the late Mesozoic global plume activity [51].

The newly obtained in situ $^{87}Sr/^{86}Sr$ isotopic compositions for dominant minerals within magnetite-apatite-enriched rocks, carbonatites, and alkaline syenites suggest limited variation, which further implies that they were derived from a common mantle source. The available experimental data provide evidence that partial melting of the upper mantle phosphate-bearing peridotite and pyroxenite can generate phosphorus-

rich melts, and these melts evolve into immiscible silicate and salt liquids at the early stages of evolution [9,55]. The oxygen isotopic compositions of apatite and phlogopite ($\delta^{18}O_{Ap}$ = 5.1–5.6‰; $\delta^{18}O_{Phl}$ = 7.3‰) from the fresh magnetite-apatite-enriched rocks reported by Nikolenko et al. [10] are typical for mantle-derived igneous rocks, which also supports their origination from the mantle [56]. Combining our newly obtained in-situ $^{87}Sr/^{86}Sr$ isotopic values with the bulk rock Nd and Pb isotope data ($^{143}Nd/^{144}Nd$ = 0.512487–0.512596, $^{206}Pb/^{204}Pb$ = 18.353–19.615, $^{207}Pb/^{204}Pb$ = 15.575–15.726, $^{208}Pb/^{204}Pb$ = 38.224–41.383) reported by Baatar et al. [6] and Nikolenko et al. [13], the Mushgai Khudag alkaline-carbonatite complex is believed to have formed from enriched mantle domains involving DMM (Depleted MORB Mantle) and EM2 (Enriched Mantle 2). Bayan Khoshuu and Lugiin Gol are the other two large carbonatite-related multi-element deposits located in Southern Mongolia, and they are also predicted to originate from similarly enriched mantle domains based on Sr–Nd isotope data [6].

6.2. Fractional Crystallization and Hydrothermal Alteration Recorded in Apatite

It is widely documented that apatite occurs through early magmatic to late hydrothermal stages and is sensitive to physical-chemical changes. It has been used as a petrogenetic and geochemical indicator for the tracing evolution of alkaline rocks [43,44]. Magmatic apatite with internal chemical variations is commonly characterized by a relatively REE-depleted core (29,963 ± 719 ppm) and an REE-enriched rim (31,963 ± 1205 ppm), which can be explained by fractional crystallization (Table S3). Apatite within syenite shows a variable REE content from the core to the rim, which is correlated with the oscillatory zonation identified on the CL images, whereas $(La/Yb)_N$ and $(La/Nd)_N$ values decrease in the core and increase in the rim (Figure 10e,f). The transition point might mark the fractional crystallization of an HREE-enriched mineral (e.g., garnet) [11]. The oscillatory zonation commonly recorded in apatite within syenite supports the significant influence of melt differentiation and accompanying fractional crystallization of feldspar and garnet in generating the variable REE features (Figure 10c–f). Magmatic apatite in magnetite-apatite-enriched rocks and syenites is characterized by negative Eu anomalies (Eu/Eu* = 0.437–0.779), similar to those present in apatite in granitic rocks [27]. Preservation of the negative Eu anomaly often indicates fractional crystallization of plagioclase and feldspar with low oxygen fugacity [12,27,57]. Thus, the geochemical features of magmatic apatite recorded from the Mushgai Khudag complex further support the fractionation of the alkaline silicate melt and the associated mineral fractional crystallization.

Magmatic apatite within magnetite-apatite-enriched rocks is characterized by near-chondritic Y/Ho ratios similar to those of the silicate rocks formed via CHArge-and-RAdius-Controlled (CHARAC) processes (Figure 9d) [45]. The variable Y/Ho ratios of altered apatite are higher than those of magmatic apatite and deviate from the chondritic value, which reflects alteration by hydrothermal fluids (Figure 9d) [49]. Oxidized U^{6+} is relatively soluble compared with U^{4+} and can be transported as phosphate or carbonate complexes in neutral and alkaline solutions [58]. The generally correlated increases in REE and U contents in altered apatite suggest that the hydrothermal fluids are possibly oxidized (Figure 8a). HREE enrichment has commonly been observed for hydrothermal apatite in Tundulu, Kangankunde, and Songwe Hill [59–61]. The HREE-enriched patterns are mostly due to the mobilization and co-precipitation of LREE minerals such as monazite and bastnäsite and/or the differing stability of REE anion complexes between LREE and HREE [59–61]. Altered apatite is commonly associated with monazite precipitation at Mushgai Khudag, as described above and observed in previous studies (Figure 3h,i) [8,10]. Nevertheless, altered apatite is still characterized by higher La/Yb_N and La/Sm_N ratios compared with magmatic apatite (Figure 9c,d), which can be generated with the contribution of extremely LREE-enriched hydrothermal fluids. Of note, altered apatite is also characterized by higher Zr/Hf (179 ± 48) and Nb/Ta (19.4 ± 10.3) ratios compared with magmatic apatite and relatively less Eu anomalies (Figure 8b,c). Carbonatite melts/fluids are known to be characterized by high Zr/Hf, Nb/Ta, and $(La/Yb)_N$ ratios without Eu

anomalies [6,13,62–65]. Thus, the late hydrothermal fluids involved in the pervasive alteration of magnetite-apatite-enriched rocks might be carbonatite exsolved. This is also supported by the fact that the Mushgai Khudag carbonatite magma originates from the common DMM-EM2 mantle domains together with magnetite-apatite-enriched rocks, as suggested by the consistent isotopic compositions outlined above. Moreover, the similarity in Sr isotopic compositions between magmatic and altered apatite also confirms that the hydrothermal fluids evolve from a common source, the same as that of the phosphorus melt. Of note, the newly obtained U–Pb ages for both magmatic and altered apatite are similar within the error range, which indicates that alterations by the carbonatite exsolved fluids probably took place almost simultaneously after the emplacement of magnetite-apatite-enriched rocks.

6.3. REE Enrichment Mechanism of the Mushgai Khudag Complex

The multi-element deposit of Mushgai Khudag is believed to have formed through multiphase liquid immiscibility based on melt and fluid inclusion studies [10,12,13]. The model involves high temperature (1250–1280 °C) carbonate-silicate melt immiscibility and relatively lower temperature (600–1200 °C) carbonate-phosphate-salt immiscibility [10,12,13,66]. The liquid immiscibility model is also supported by our newly obtained U–Pb ages of magnetite-apatite-enriched rocks that are consistent with alkaline silicate rocks and carbonatite and similar Sr isotopic compositions for various rock types, as mentioned above. In an aqueous carbonate-phosphate-silicate melt system, REEs favor carbonate melt during carbonate-silicate liquid immiscibility and phosphate melt during phosphate-silicate liquid immiscibility [67,68]. This is evidenced by the lower REE content in syenite (716 ± 241 ppm) compared with in magnetite-apatite-enriched rocks (28,681 ± 6752 ppm) and carbonatites (26,692 ppm). Moreover, apatite is one of the predominant minerals controlling the REE budget in these rocks. Apatite within syenite and shonkinite also shows a lower REE concentration compared to apatite within magnetite-apatite-enriched rocks (Table S3) [13,67,68]. Magmatic apatite hosting the extremely enriched REE contents (up to 7.0 wt.%; Table S3) in magnetite-apatite-enriched rock suggests that REEs also favor phosphate melt during phosphate-salt immiscibility. Magmatic apatite within magnetite-apatite-enriched rock and syenite exhibits a positive correlation between LREE and Si abundance, which suggests that the coupled substitution scheme of $Si^{4+} + REE^{3+} = P^{5+} + Ca^{2+}$ plays the dominant role in REE incorporation within the apatite during magmatic evolution [26].

The bulk rock SO_3 content of the altered magnetite-apatite-enriched rocks is almost twice that in fresh ones (Table S1). Altered apatite in these altered rocks is more abundant in SO_3 compared to in magmatic apatite and is also much higher than the sulfur content of apatite within other magnetite-apatite-enriched rocks, e.g., El Laco (S: 155–4791 ppm; [14]) and Carmen (SO_3: 0.01–2.39 wt.%; [25]). The correlated increases in S and Si contents together with LREE enrichment in Ap-4 indicates that both the substitution schemes of $Si^{4+} + REE^{3+} = P^{5+} + Ca^{2+}$ and $S^{6+} + REE^{3+} = P^{5+} + 2Ca^{2+}$ contribute to the incorporation of REE into altered apatite. In addition, the SO_3 content of secondary monazite within the altered Mushgai Khudag magnetite-apatite-enriched rocks (0.56–9.94 wt.%; [8,10]) is much higher than that of other carbonatites and magnetite-apatite-enriched rocks (0.15–1.72 wt.%; [69–73]), which also supports the idea that sulfate plays an important role in REE mobility during alterations. In other words, the unusual sulfur enrichments in altered apatite and deposited monazite indicate that sulfate is an important ligand for REE transportation [74,75]. Of note, experimental work suggests that differences in the stability of LREE and HREE as aqueous chloride complexes can result in REE fractionation, whereas LREE and HREE transported as sulfate complexes show similar levels of stability [74–77]. Thus, compared with the preferred mobility of LREE as a chloride complex, sulfate-dominated fluids possibly result in relative HREE enrichment during hydrothermal processes, such as those observed in Songwe Hill apatite [27,76,77]. The altered Mushgai Khudag apatite with depleted HREE and high $(La/Yb)_N$ ratios implies that the REE patterns of altered apatite are dominantly

controlled by LREE-enriched carbonatite-evolved fluids, and the different REE ligands play a limited role in REE fractionation during the pervasive hydrothermal alteration at Mushgai Khudag.

7. Conclusions

The newly obtained, consistent in situ U–Pb ages of magmatic and altered apatite (139.7 ± 2.6 and 138.0 ± 1.3 Ma, respectively) within the Mushgai Khudag magnetite-apatite-enriched rocks support the presence of late Mesozoic alkaline-carbonatite magmatism and indicate that pervasive alterations probably took place almost simultaneously after the magmatism. In situ $^{87}Sr/^{86}Sr$ isotopic values (0.70572–0.70648) within the reported bulk rock Nd and Pb isotope data suggest that the Mushgai Khudag complex originated from the mantle, involving both DMM and EM2 reservoirs. The variable trace element compositions (especially the REE patterns) and texture of magmatic apatite from both magnetite-apatite-enriched rocks and syenites show melt differentiation and mineral fractional crystallization. Altered apatite is characterized by higher REE, U, Nb/Ta, Zr/Hf, and $(La/Yb)_N$ values and a lack of Eu anomalies compared with magmatic apatite, which suggests that the carbonatite-exsolved LREE-bearing fluids overprinting magnetite-apatite-enriched rocks further contribute to REE enrichment with monazite precipitation. The coupled increases in sulfur and LREE contents in altered apatite (Ap-4) associated with sulfur-enriched secondary monazite indicate that sulfate plays an important role in REE transportation and mineralization during hydrothermal alteration at the Mushgai Khudag deposit.

Supplementary Materials: The following are available online at https://www.mdpi.com/article/10.3390/min11050450/s1. Table S1. Chemical compositions for magnetite-apatite-enriched rock, syenite and carbonatite from Mushgai Khudag; Table S2. Mineral compositions for apatite within magnetite-apatite-enriched rocks and syenite from Mushgai Khudag; Table S3. Trace element compositions (ppm) for carbonatite within carbonatite from Mushgai Khudag; Table S4. U-Pb ages for magmatic and altered apatite within magnetite-apatite-enriched rocks from Mushgai Khudag; Table S5. In-situ Sr isotope compositions for apatite within magnetite-apatite-enriched rocks and syenite and calcite within carbonatite from Mushgai Khudag.

Author Contributions: Conceptualization, W.C. and F.Y.; methodology, software and validation, F.Y.; formal analysis and investigation F.Y., Y.Y. and T.B.; resources, W.C. and J.K.; data curation, F.Y.; writing—original draft preparation, F.Y.; writing—review and editing, W.C.; visualization, W.C. and F.Y.; supervision, W.C.; project administration, W.C. and J.K.; funding acquisition, W.C. and J.K. All authors have read and agreed to the published version of the manuscript.

Funding: This research was funded by the National Key R&D Program of China (No. 2019YFA0708400), the National Natural Science Foundation of China (Nos. 41973016, 41530211) and EXPRO 2019 project of the The Czech Science Foundation (no.19-29124X).

Data Availability Statement: The data presented in this study are available on request from the corresponding author.

Acknowledgments: Samples were taken during the 2016 and 2017 HiTech AlkCarb Mongolian Alkaline Rock field trips. The authors would like to express their sincere gratitude to the editors and the anonymous reviewers for their helpful remarks and constructive comments, which have improved the quality of the paper.

Conflicts of Interest: The authors declare no conflict of interest.

References

1. European Commission. *Report on Critical Raw Materials and the Circular Economy*; European Commission: Brussels, Belgium, 2018.
2. Smith, M.P.; Moore, K.; Kavecsanszki, D.; Finch, A.A.; Kynicky, J.; Wall, F. From mantle to critical zone: A review of large and giant sized deposits of the rare earth elements. *Geosci. Front.* **2016**, *7*, 315–334. [CrossRef]
3. Chen, W.; Liu, H.Y.; Lu, J.; Jiang, S.Y.; Simonetti, A.; Xu, C.; Zhang, W. The formation of the ore-bearing dolomite marble from the giant Bayan Obo REE-Nb-Fe deposit, Inner Mongolia: Insights from micron-scale geochemical data. *Miner. Depos.* **2019**, *55*, 131–146. [CrossRef]

4. Liu, Y.; Zhu, Z.M.; Chen, C.; Zhang, S.P.; Sun, X.; Yang, Z.S.; Liang, E. Geochemical and mineralogical characteristics of weathered ore in the Dalucao REE deposit, Mianning-Dechang REE Belt, western Sichuan Province, southwestern China. *Ore Geol. Rev.* **2015**, *71*, 437–456. [CrossRef]
5. Poletti, J.E.; Cottle, J.M.; Hagen-Peter, G.A.; Lackey, J.S. Petrochronological constraints on the origin of Mountain Pass ultrapotassic and carbonatite intrusive suite, California. *J. Petrol.* **2016**, *57*, 1555–1598. [CrossRef]
6. Baatar, M.; Ochir, G.; Kynicky, J.; Iizumi, S.; Comin-Chiaramonti, P. Some notes on the Lugiin Gol, Mushgai Khudag and Bayan Khoshu alkaline complexes, Southern Mongolia. *Int. J. Geosci.* **2013**, *4*, 1200–1214. [CrossRef]
7. Smith, M.P.; Campbell, L.S.; Kynicky, J. A review of the genesis of the world class Bayan Obo Fe-REE-Nb deposits, Inner Mongolia, China: Multistage processes and outstanding questions. *Ore Geol. Rev.* **2015**, *64*, 459–476. [CrossRef]
8. Enkhbayar, D.; Seo, J.; Choi, S.G.; Lee, Y.J.; Batmunkh, E. Mineral chemistry of REE-rich apatite and sulfur-rich monazite from the Mushgai Khudag, alkaline volcanic-plutonic complex, South Mongolia. *Int. J. Geosci.* **2016**, *7*, 20–31. [CrossRef]
9. Andreeva, I.A.; Kovalenko, V.I. Magma compositions and genesis of the rocks of the Mushugai-Khuduk carbonatite-bearing alkaline complex (southern Mongolia): Evidence from melt inclusions. *Per. Mineral.* **2003**, *72*, 95–105.
10. Nikolenko, A.M.; Redina, A.A.; Doroshkevich, A.G.; Prokopyev, I.R.; Ragozin, A.L.; Vladykin, N.V. The origin of magnetite-apatite rocks of Mushgai-Khudag Complex, South Mongolia: Mineral chemistry and studies of melt and fluid inclusions. *Lithos* **2018**, *320–321*, 567–582. [CrossRef]
11. Samoilov, V.S.; Kovalenko, V.I. *Complexes of Alkaline Rocks and Carbonatites in South Mongolia*; Nauka: Moscow, Russia, 1983.
12. Andreeva, I.A.; Kovalenko, V.I.; Naumov, V.B. Silicate-salt (sulfate) liquid immiscibility: A study of melt inclusions in minerals of the Mushgai-Khuduk carbonatite-bearing complex (southern Mongolia). *Acta Petrol. Sin.* **2017**, *23*, 73–82.
13. Nikolenko, A.M.; Doroshkevich, A.G.; Ponomarchuk, A.V.; Redina, A.A.; Prokopyev, I.R.; Vladykin, N.V.; Nikolaeva, I.V. Ar-Ar geochronology and petrogenesis of the Mushgai-Khudag alkaline-carbonatite complex (southern Mongolia). *Lithos* **2020**, *372–373*, 105675. [CrossRef]
14. La Cruz, N.L.; Ovalle, J.T.; Simon, A.C.; Konecke, B.A.; Childress, T.M. The geochemistry of magnetite and apatite from the El Laco iron oxide-apatite deposit, Chile: Implications for ore genesis. *Econ. Geol.* **2020**, *115*, 1461–1491. [CrossRef]
15. Frietsch, R.; Perdahl, J.A. Rare earth element in apatite and magnetite in Kiruna-type iron ores and some other iron ore types. *Ore Geol. Rev.* **1995**, *9*, 489–510. [CrossRef]
16. Harlov, D.E.; Meighan, C.J.; Kerr, I.D.; Samson, I.M. Mineralogy, chemistry and fluid-aided evolution of the Pea Ridge Fe oxide-(Y+REE) deposit, Southeast Missouri, USA. *Econ. Geol.* **2016**, *111*, 1963–1984. [CrossRef]
17. Chen, H.; Clark, A.H.; Kyser, T.K. The Marconamagnetite deposit, Ica, south-central Peru: A product of hydrous, iron oxide-rich melts? *Econ. Geol.* **2010**, *105*, 1441–1456. [CrossRef]
18. VanTongeren, J.A.; Mathez, E.A. Large-scale liquid immiscibility at the top of the Bushveld Complex, South Africa. *Geology* **2012**, *40*, 491–494. [CrossRef]
19. Velasco, F.; Tornos, F.; Hanchar, J.M. Immiscible iron-and silicarich melts and magnetite geochemistry at the El Laco volcano (northern Chile): Evidence for a magmatic origin for the magnetite deposits. *Ore Geol. Rev.* **2016**, *79*, 346–366. [CrossRef]
20. Hou, T.; Charlier, B.; Holtz, F.; Veksler, I.; Zhang, Z.; Thomas, R.; Namur, O. Immiscible hydrous Fe–Ca–P melt and the origin of iron oxide-apatite ore deposits. *Nat. Commun.* **2018**, *9*, 1415. [CrossRef]
21. Sillitoe, R.H.; Burrows, D.R. New field evidence bearing on the origin of the El Laco magnetite deposit, northern Chile. *Econ. Geol.* **2002**, *97*, 1101–1109.
22. Dare, S.; Barnes, S.J.; Beaudoin, G. Did the massive magnetite "lava flows" of El Laco (Chile) form by magmatic or hydrothermal processes? New constraints from magnetite composition LA-ICP-MS. *Miner. Depos.* **2015**, *50*, 607. [CrossRef]
23. Knipping, J.L.; Bilenker, L.D.; Simon, A.C.; Reich, M.; Barra, F.; Deditius, A.P.; Lundstrom, C.; Bindeman, I.; Munizaga, R. Giant Kiruna-type deposits form by efficient flotation of magmatic magnetite suspensions. *Geology* **2015**, *43*, 591–594. [CrossRef]
24. Knipping, J.L.; Bilenker, L.D.; Simon, A.C.; Reich, M.; Barra, F.; Deditius, A.P.; Wälle, M.; Heinrich, C.A.; Holtz, F.; Munizaga, R. Trace elements in magnetite from massive iron oxide-apatite deposits indicate a combined formation by igneous and magmatic-hydrothermal processes. *Geochim. Cosmochim. Acta* **2005**, *171*, 15–38. [CrossRef]
25. Palma, G.; Barra, F.; Reich, M.; Valencia, V.; Simon, A.C.; Vervoort, J.; Leisen, M.; Romero, R. Halogens (F, Cl, OH), trace element contents, and Sr-Nd isotopes in apatite from iron oxide-apatite (IOA) deposits in the Chilean iron belt: Evidence for magmatic and hydrothermal stages of mineralization. *Geochim. Cosmochim. Acta* **2019**, *246*, 515–540. [CrossRef]
26. Pan, Y.; Fleet, M.E. Compositions of the apatite-group minerals: Substitution mechanisms and controlling factors. *Rev. Mineral. Geochem.* **2002**, *48*, 13–49. [CrossRef]
27. Mao, M.; Rukhlov, A.S.; Rowins, S.M.; Spence, J.; Coogan, L.A. Apatite trace element compositions: A robust new tool for mineral exploration. *Econ. Geol.* **2016**, *111*, 1187–1222. [CrossRef]
28. Harlov, D.E. Apatite: A fingerprint for metasomatic processes. *Elements* **2015**, *11*, 171–176. [CrossRef]
29. Nathwani, C.L.; Loader, M.A.; Wilkinson, J.J.; Buret, Y.; Sievwright, R.H.; Hollings, P. Multi-stage arc magma evolution recorded by apatite in volcanic rocks. *Geology* **2020**, *48*, 323–327. [CrossRef]
30. O'Sullivan, G.; Chew, D.; Kenny, G.; Henrichs, I.; Mulligan, D. The trace element composition of apatite and its application to detrital provenance studies. *Earth Sci. Rev.* **2020**, *201*, 103044. [CrossRef]

31. Liu, Y.S.; Zong, K.Q.; Kelemen, P.B.; Gao, S. Geochemistry and magmatic history of eclogites and ultramafic rocks from the Chinese continental scientific drill hole: Subduction and ultrahigh-pressure metamorphism of lower crustal cumulates. *Chem. Geol.* **2008**, *247*, 133–153. [CrossRef]
32. Ketcham, R.A. Technical Note: Calculation of stoichiometry from EMP data for apatite and other phases with mixing on monovalent anion sites. *Am. Mineral.* **2015**, *100*, 1620–1623. [CrossRef]
33. Liu, Y.S.; Hu, Z.C.; Gao, S.; Günther, D.; Xu, J.; Gao, C.G.; Chen, H.H. In situ analysis of major and trace elements of anhydrous minerals by LA-ICP-MS without applying an internal standard. *Chem. Geol.* **2008**, *257*, 34–43. [CrossRef]
34. Chen, W.; Simonetti, A. In-situ determination of major and trace elements in calcite and apatite, and U-Pb ages of apatite from the Oka carbonatite complex: Insights into a complex crystallization history. *Chem. Geol.* **2013**, *353*, 151–172. [CrossRef]
35. Thomson, S.N.; Gehrels, G.E.; Cecil, R.; Ruiz, J. Exploring routine laser ablation multicollector ICP-MS U-Pb dating of apatite. In Proceedings of the American Geophysical Union (AGU) Fall Meeting, San Francisco, CA, USA, 14–18 December 2009.
36. Ludwig, K.R. *User's Manual for Isoplot 3.00: A Geochronological Toolkit for Microsoft Excel*; Berkeley Geochronology Center: Berkeley, CA, USA, 2003.
37. Chen, W.; Simonetti, A. Evidence for the multi-stage petrogenetic history of the Oka carbonatite complex (Québec, Canada) as recorded by perovskite and apatite. *Minerals* **2014**, *4*, 437–476. [CrossRef]
38. Pu, W.; Gao, J.F.; Zhao, K.D.; Ling, H.F.; Jiang, S.Y. Separation method of Rb-Sr, Sm-Nd using DCTA and HIBA. *J. Nanjing Univ.* **2005**, *41*, 445–450, (In Chinese with English abstract).
39. McDonough, W.F.; Sun, S.S. The Composition of the Earth. *Chem. Geol.* **1995**, *120*, 223–253. [CrossRef]
40. Sun, S.; McDonough, W.F. Chemical and Isotopic Systematics of Oceanic Basalts Implications for Mantle Composition and Processes. *Geol. Soc. Lond. Spec. Publ.* **1989**, *42*, 313–345. [CrossRef]
41. Middlemost, E.A.K. Naming Materials in the Magma/Igneous Rock System. *Earth Sci. Rev.* **1994**, *37*, 215–224. [CrossRef]
42. Woolley, A.R.; Kempe, E.R.C. Carbonatites: Nomenclature, average chemical compositions, and element distribution. In *Carbonatites: Genesis and Evolution*; Bell, K., Ed.; Unwin-Hyman: London, UK, 1989; pp. 1–14.
43. Bühn, B.; Wall, F.; Le Bas, M.J. Rare-earth element systematic of carbonatitic fluorapatites and their significance for carbonatite magma evolution. *Contrib. Mineral. Petrol.* **2001**, *141*, 572–591. [CrossRef]
44. Chakhmouradian, A.R.; Regui, E.P.; Zaitsev, A.N.; Couëslan, C.; Xu, C.; Kynický, J.; Mumin, A.H.; Yang, P. Apatite in carbonatitic rocks: Compositional variation, zoning, element partitioning and petrogenetic significance. *Lithos* **2017**, *274–275*, 188–213. [CrossRef]
45. Bau, M. Controls on the fractionation of isovalent trace elements in magmatic and aqueous systems: Evidence from Y/Ho, Zr/Hf, and lanthanide tetrad effect. *Contrib. Mineral. Petrol.* **1996**, *123*, 323–333. [CrossRef]
46. Broom-Fendley, S.; Brady, A.E.; Wall, F.; Gunn, G.; Dawes, W. REE minerals at the Songwe Hill carbonatite, Malawi: HREE-enrichment in late-stage apatite. *Ore Geol. Rev.* **2017**, *81*, 23–41. [CrossRef]
47. Chakhmouradian, A.R.; Reguir, E.P.; Coueslan, C.; Yang, P. Calcite and dolomite in intrusive carbonatites II. Trace-element variations. *Miner. Petrol.* **2016**, *110*, 361–377. [CrossRef]
48. Halama, R.; Vennemann, T.W.; Siebel, W.; Markl, G. The Grønnedal–Ika carbonatite–syenite complex, South Greenland: Carbonatite formation by liquid immiscibility. *J. Petrol.* **2005**, *46*, 191–217. [CrossRef]
49. Wu, F.Y.; Yang, Y.H.; Li, Q.L.; Mitchell, R.H.; Dawson, J.B.; Brandl, G.; Yuhara, M. In situ determination of U-Pb ages and Sr-Nd-Hf isotopic constraints on the petrogenesis of the Phalaborwa carbonatite Complex, South Africa. *Lithos* **2011**, *127*, 309–322. [CrossRef]
50. Kempe, U.; Gotze, J. Cathodoluminescence (CL) behaviour and crystal chemistry of apatite from rare-metal deposits. *Mineral. Mag.* **2002**, *66*, 151–172. [CrossRef]
51. Nikiforov, A.V.; Yarmolyuk, V.V. Late Mesozoic carbonatite provinces in Central Asia: Their compositions, sources and genetic settings. *Gondw. Res.* **2019**, *69*, 56–72. [CrossRef]
52. Nikiforov, A.V.; Bolonin, A.V.; Chugaev, A.V.; Lykhin, D.A.; Pokrovsky, B.G.; Sugorakova, A.M. Isotope geochemistry (O, C, S, Sr) and Rb-Sr age of carbonatites in central Tuva. *Geol. Ore Dep.* **2006**, *48*, 256–276. [CrossRef]
53. Ripp, G.S.; Doroshkevich, A.G.; Posokhov, V.F. Age of carbonatite magmatism in Transbaikalia. *Petrology* **2009**, *17*, 73–89. [CrossRef]
54. Prokopyev, I.R.; Borisenko, A.S.; Borovikov, A.A.; Pavlova, G.G. Origin of REE-rich ferrocarbonatites in southern Siberia (Russia): Implications based on melt and fluid inclusions. *Mineral. Petrol.* **2016**, *110*, 845–859. [CrossRef]
55. Kogarko, L.N.; Ryabchikov, I.D. Phosphorus in the processes of magma melting. *Dokl. Akad. Nauk SSSR* **1983**, *269*, 1192–1194.
56. Hoefs, J. *Stable Isotope Geochemistry*; Springer International Publishing, AG: Basel, Switzerland, 2015.
57. Zhang, X.B.; Guo, F.; Zhang, B.; Zhao, L.; Wu, Y.M.; Wang, G.Q.; Alemayehu, M. Magmatic evolution and post-crystallization hydrothermal activity in the early Cretaceous Pingtan intrusive complex, SE China: Records from apatite geochemistry. *Contrib. Mineral. Petrol.* **2020**, *175*, 25. [CrossRef]
58. Nash, B.P.; Crecraft, H. Partition coefficients for trace elements in silicic magmas. *Geochim. Cosmochim. Acta* **1985**, *49*, 2309–2322. [CrossRef]
59. Langmuir, C.H. Geochemical consequences of in situ crysallization. *Nature* **1989**, *340*, 199–205. [CrossRef]

60. Broom-Fendley, S.; Heaton, T.; Wall, F.; Gunn, G. Tracing the fluid source of heavy REE mineralisation in carbonatites using a novel method of oxygen-isotope analysis in apatite: The example of Songwe Hill, Malawi. *Chem. Geol.* **2016**, *440*, 275–287. [CrossRef]
61. Broom-Fendley, S.; Styles, M.T.; Appleton, J.D.; Gunn, G.; Wall, F. Evidence for dissolution-reprecipitation of apatite and preferential LREE mobility in carbonatite-derived late-stage hydrothermal processes. *Am. Mineral.* **2016**, *101*, 596–611. [CrossRef]
62. Taylor, S.R.; McLennan, S.M. *The Continental Crust: Its Composition and Evolution: An Examination of the Geochemical Record Preserved in Sedimentary Rocks*; Blackwell Science: Oxford, UK, 1985.
63. Buchl, A.; Brugmann, G.; Batanova, V.G.; Munker, C.; Hofmann, A.W. Melt percolation monitored by Os isotopes and HSE abundances: A case study from the mantle section of the Troodos Ophiolite. *Earth Planet. Sci. Lett.* **2001**, *204*, 385–402. [CrossRef]
64. Munker, C.; Pfander, J.A.; Weyer, S.; Buchl, A.; Kleine, T.; Mezger, K. Evolution of planetary cores and the earth–moon system from Nb/Ta systematics. *Science* **2003**, *301*, 84–87. [CrossRef]
65. Rudnick, R.L.; Gao, S. Composition of the continental crust. *Treatise Geochem.* **2004**, *3*, 1–65.
66. Panina, L.I.; Motorina, I.V. Liquid immiscibility in deep-seated magmas and the generation of carbonatite melts. *Geochem. Int.* **2008**, *46*, 448–464. [CrossRef]
67. Veksler, I.V.; Dorfman, A.M.; Dulski, P.; Kamenetsky, V.S.; Danyushevsky, L.V.; Jeffries, T.; Dingwell, D.B. Partitioning of elements between silicate melt and immiscible fluoride, chloride, carbonate, phosphate and sulfate melts, with implications to the origin of natrocarbonatite. *Geochim. Cosmochim. Acta* **2012**, *79*, 20–40. [CrossRef]
68. Martin, L.H.J.; Schmidt, M.W.; Mattsson, H.B.; Guenther, D. Element partitioning between immiscible carbonatite and silicate melts for dry and H_2O-bearing systems at 1–3GPa. *J. Petrol.* **2013**, *54*, 2301–2338. [CrossRef]
69. Kim, S.J.; Lee, H.K.; Yin, J.; Park, J.K. Chemistry and origin of monazites from carbonatite dikes in the Hongcheon–Jaeun district, Korea. *J. Asian Earth Sci.* **2005**, *25*, 57–67. [CrossRef]
70. Doroshkevich, A.G.; Ripp, G.S.; Moore, K.R. Genesis of the Khaluta alkaline-basic Ba-S rcarbonatite complex (West Transbaikala, Russia). *Mineral. Petrol.* **2010**, *98*, 245–268. [CrossRef]
71. Xu, C.; Kynicky, J.; Chakhmouradian, A.R.; Qi, L.; Song, W.L. A unique Mo deposit associated with carbonatites in the Qinling orogenic belt, central China. *Lithos* **2010**, *118*, 50–60. [CrossRef]
72. Prokopyev, I.R.; Doroshkevich, A.G.; Ponomarchuk, A.V.; Sergeev, S.A. Mineralogy, age and genesis of apatite-dolomite ores at the Seligdar apatite deposit (Central Aldan, Russia). *Ore Geol. Rev.* **2017**, *81*, 296–308. [CrossRef]
73. Xie, Y.L.; Li, Y.X.; Hou, Z.Q.; David, R.C.; Leonid, D.; Simon, C.D.; Yin, S.P. A model for carbonatite hosted REE mineralization-the Mianning-Dechang REE belt, Western Sichuan Province, China. *Ore Geol. Rev.* **2015**, *70*, 595–612. [CrossRef]
74. Migdisov, A.A.; Williams-Jones, A.E.; Brugger, J.; Caporuscio, F.A. Hydrothermal transport, deposition, and fractionation of the REE: Experimental data and thermodynamic calculations. *Chem. Geol.* **2016**, *439*, 13–42. [CrossRef]
75. Migdisov, A.A.; Williams-Jones, A.E. A spectrophotometric study of Nd(III), Sm(III) and Er(III) complexation in sulfate-bearing solutions at elevated temperatures. *Geochim. Cosmochim. Acta* **2008**, *72*, 5291–5303. [CrossRef]
76. Migdisov, A.A.; Williams-Jones, A.E.; Wagner, T. An experimental study of the solubility and speciation of the rare earth elements (III) in fluoride-and chloride-bearing aqueous solutions at temperatures up to 300 °C. *Geochim. Cosmochim. Acta* **2009**, *73*, 7087–7109. [CrossRef]
77. Williams-Jones, A.; Migdisov, A.; Samson, I. Hydrothermal mobilisation of the rare earth elements: A tale of "Ceria" and "Yttria". *Elements* **2012**, *8*, 355. [CrossRef]